PHOTOEMISSION

Photoemission spectroscopy has been an active area of research for almost a century. Einstein's explanation of the photoelectric effect was one of the early triumphs of the quantum theory and earned him the Nobel prize. Even upon its initial observation, researchers realized that the photoelectric effect can provide important information about material properties. In the ensuing years, the energy and angular distributions of electrons photoemitted from solids have been investigated with increasing interest. With the recent construction of "third-generation" synchrotron radiation facilities that may be used as high-intensity, high-resolution, variable-energy photon sources, there is no sign of this activity waning.

The tremendous utility of photoemission as a tool for materials analysis comes from the fact that the kinetic energy distribution of primary features in a photoemission spectrum is directly related to the energy distribution of electrons in the solid prior to photoexcitation. Since electronic structure governs all physical, chemical, electrical, and magnetic properties of a solid, photoemission can provide the essential underpinning to our understanding of how materials function in practical applications. Moreover, most primary photoelectrons originate within 1 nm to 2 nm of the sample surface. As the critical dimension of a widening array of devices approaches nanometer length scales, the region most directly probed by photoemission is increasingly relevant. Even in applications that do not demand materials control with nanometer tolerances, the interaction of a solid with its environment occurs through the window of the surface. Understanding the nature of this window is essential to understanding and predicting device performance.

In this article, the basic processes and mechanisms of photoemission are described, along with many of the most common applications for materials analysis. We refer the reader to the bibliography for more extensive discussions of the topics addressed in this work. We note that this list is a representative sampling of the literature in the field and is by no means intended to be an exhaustive compilation. In the section entitled "The Basic Properties of the Photoemission Spectrum," the basic properties of the photoemission spectrum are discussed. The section entitled "Experimental Considerations" describes experimental implementation of the technique, while the section entitled "Elementary Principles of Photoemission" addresses the elementary principles of photoemission. Finally, in the section entitled "Applications of Photoemission," the most common uses of photoemission spectroscopy are discussed, including core-level, valence-band, spin-polarized, and angle-resolved photoemission as well as inverse photoemission spectroscopy.

THE BASIC PROPERTIES OF THE PHOTOEMISSION SPECTRUM

The close relationship between the photoemission spectrum and the electronic states of a solid is illustrated in Fig. 1.

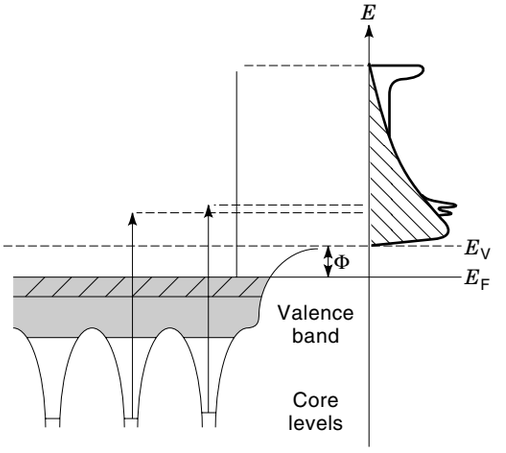

Figure 1. The relationship of photoelectrons to the electronic structure of a solid. Energetically, the electronic states of a solid can be divided into two types, the loosely bound valence levels and the tightly bound core levels. If an electron of the solid is excited by a photon of sufficient energy, the electron will be emitted as a photoelectron. Since all the energy of the photon is given to the photoelectron, one can directly relate the kinetic energy distribution of photoelectrons to the energy distribution of electrons in the solid.

Typically, the occupied states are conceptually divided into two parts: (1) the valence band, which contains the electrons that determine the bonding, chemical, electrical, optical, and magnetic properties of the solid, and (2) the core levels, which are filled, largely inert orbitals which, even in the solid state environment, are only moderately changed from their atomic character. When an ultraviolet (UV) or X-ray photon is absorbed by an atom in a solid, an electron is excited and, if it has sufficient energy, may escape the solid. This emitted electron is called a photoelectron.

Figure 1 shows how the kinetic energy of a photoelectron is related to the energy of the electron before excitation. To a first approximation, there are two contributions to the kinetic energy distribution of emitted electrons: primary emission and secondary emission. Primary emission consists of those photoelectrons that escape the solid without suffering inelastic collisions. Secondary emission contains electrons that have lost energy before emerging from the solid. Primary photoemission typically is superimposed on a background of secondary electrons. In principle, it is not possible to distinguish between primary and secondary electrons on an event-by-event basis. However, in most applications a practical background can be established and subsequently removed from the spectrum, leaving the primary features to be analyzed. We confine our discussion to primary photoelectrons.

Measured with respect to the vacuum level of the solid, E_V, the maximum kinetic energy of the photoelectron, $E_{K_{max}}$, differs from the photon energy by an amount equal to the work function Φ:

$$E_{K_{max}} = \hbar\omega - \Phi \tag{1}$$

Equation (1) is the famous Einstein relation, where Φ represents the work function, that is the minimum energy needed by an electron to overcome the surface potential barrier and escape the sample. As indicated in the figure, all other primary electrons have less kinetic energy than those originating from E_F. The difference between the high energy cut off of the spectrum and the kinetic energy of an emitted primary electron is called the binding energy:

$$E_B = (\hbar\omega - \Phi) - E_K \tag{2}$$

As indicated by Fig. 1, the binding energy is associated with the energy of the electron prior to excitation. Typically, less energy is required to eject an electron from the valence band, so often a UV photon is employed and one speaks of ultraviolet photoemission spectroscopy (UPS). To study core levels, excitation by X rays is typically needed and the associated analytical technique is called X-ray photoelectron spectroscopy (XPS). The possible sensitivity of core-level binding energy to the environment of the atom is indicated by an energy shift of the surface core level.

Two other photoelectron-based techniques, Auger electron spectroscopy (AES) and inverse photoemission (IPE) spectroscopy, are summarized in Fig. 2. The Auger effect is a relaxation process initiated by the creation of a core hole. If the core hole in the atom has energy E_c, and the two holes left in the final state have energies E_i and E_j, then energy balance gives $E_i + E_j + E_A = E_c$, where E_A is the kinetic energy of the Auger electron. Solving for E_A we find $E_A = E_c - (E_i + E_j)$. This relationship shows that the kinetic energy of the Auger electron is independent of how the core hole is created. As such, an Auger feature can be identified in a photoemission spectrum because its kinetic energy is independent of the

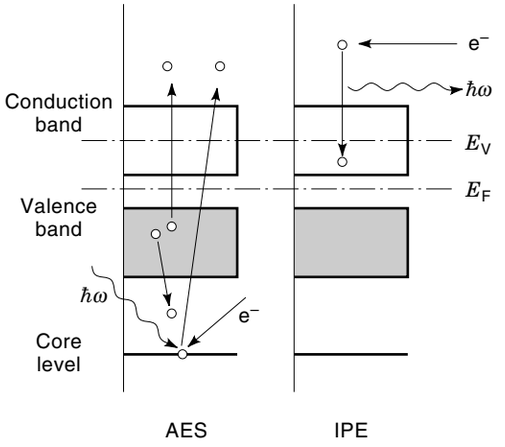

Figure 2. A schematic energy diagram of Auger electron spectroscopy (AES) and inverse photoemission spectroscopy (IPE). In AES a core hole is excited either by photoemission or electron bombardment. In the subsequent Auger decay process, a less tightly bound electron drops into the core hole and a second electron is emitted to conserve energy. Illustrated in this figure is a core-valence-valence (CVV) Auger transition where the two electrons involved in the decay originate in the valence band. In IPE, an electron that is incident on the sample couples to high-lying unoccupied states. It then may decay to a lower-lying unoccupied state by emission of a photon. In IPE, one measures the intensity distribution of photon energies generated by the decay of electrons of a fixed energy, or else one measures the intensity of photons at a fixed energy (usually in the vacuum ultraviolet range) as a function of incident electron energy. The inverse photoemission spectrum maps the unoccupied electronic states of a solid much as photoemission maps the occupied levels.

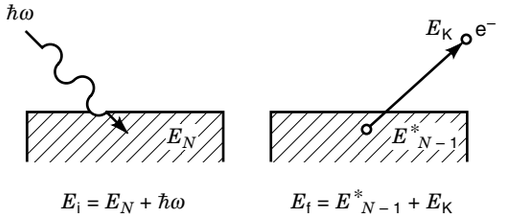

Figure 3. A schematic representation of the photoexcitation of a solid. The initial state is an N-electron solid in its ground state and a photon. The final state is an $(N - 1)$ electron ion plus the emitted photoelectron. It is important to remember that photoemission probes the excited states of a solid. Therefore, any connection between the photoemission spectrum of a solid and its properties of a solid requires several approximations.

photon energy. We note here that the initial core hole excitation is often accomplished by electron excitation where an incident electron has kinetic energy in the range of 2 keV to 3 keV. Although electron excitation of Auger electrons often is simpler experimentally than photoexcitation, the Auger spectrum contains a larger background of inelastic electrons often necessitating modulation techniques to extract the signal.

The energetics of IPE is also shown in Fig. 2. Although we will discuss it in more detail later, we only briefly mention inverse photoemission here. In IPE, an incident electron enters a high-lying unoccupied state of the sample and then makes a transition to a lower-energy conduction band state by the emission of a photon. Note that IPE can provide information about the electronic states between the Fermi level and the vacuum level, an energy region that cannot be probed by photoemission since the electron cannot escape the solid. These states are of key importance since the conduction bands of semiconductors and the minority spin states in magnetic systems fall in this energy range.

As a final point in this introductory section, the reader is reminded that in principle, photoemission is an ion spectroscopy and does not probe the ground state of the solid. As illustrated in Fig. 3, the initial state consists of a solid containing N electrons with ground state energy E_N, and an incident photon of energy $\hbar\omega$. The final state is comprised of the solid in an $N - 1$ electron ionic state of energy E^*_{N-1}, along with a photoelectron of kinetic energy E_K. Energy conservation requires that final total energy of the system equal the initial total energy, that is, $E_f = E_i$. Substituting in this expression yields

$$E_N + \hbar\omega = E^*_{N-1} + E_K \tag{3}$$

Solving for the quantity $E^*_{N-1} - E_N$ gives

$$(E^*_{N-1} - E_N) = \hbar\omega - E_K \tag{4}$$

Modulo the work function, the quantity $E^*_{N-1} - E_N$ is the binding energy E_B quoted above. Therefore, the binding energy is in principle the difference between an excited ionic state of the $N - 1$ particle system and the ground state of the initial N-particle system. It can be shown that within the frozen orbital approximation of Hartree–Fock theory, this energy difference is exactly equal to the energy eigenvalue of the empty orbital. This observation, known as Koopmans' theorem (1), has been the theoretical justification for associating photoelectron binding energies with ground-state orbital energies in atoms and solids. Although it is an approximation in principle, in most circumstances the binding energy can be associated with electron energy levels of the solid.

EXPERIMENTAL CONSIDERATIONS

The minimal experimental requirements of photoemission spectroscopy are (1) excitation of the sample by monochromatic UV or X-ray photons and (2) energy (and perhaps emission angle) analysis of the emitted photoelectrons. Typically, soft X-rays are used to excite the sample, resulting in photoelectron kinetic energies in the 10 eV to 1000 eV range. Figure 4 (2) shows a plot of electron mean free path (MFP) as a function of kinetic energy for a large collection of solids. This so-called universal curve shows that in the kinetic energy range typical of photoelectrons (10 eV $\lesssim$ KE $\lesssim$ 1000 eV), escape depths are subnanometer and hence photoemission is a surface-sensitive technique. This has the advantage of enabling one to examine the surface properties of a solid, but it also imposes the additional constraint that, to prevent sample contamination, experiments must be performed in an ultrahigh vacuum (UHV) environment. Consequently, the sample, photon source, and electron analyzer are typically housed in a vacuum chamber capable of reaching a pressure of 10^{-9} torr or lower. Furthermore, sample manipulation or treatment, as well as any electrical, mechanical, or fluid requirements of the apparatus, must be provided by hermetically sealed feedthroughs, and only UHV-compatible materials may be used within the chamber. The chamber itself is typically constructed of stainless steel, and internal components are usually nonporous metals or oxides with extremely low vapor pressures. To facilitate sample introduction into the UHV environment, experimental chambers are connected to small preparation chambers that can be rapidly isolated and evacuated. By this method, the sample chamber will experience only a brief pressure rise when a new sample is inserted.

In almost any variation of the photoemission experiment, the sample is excited with monochromatic photons. Three types of photon sources are most commonly used: gas discharge lamps, X-ray anodes, and synchrotron radiation sources. A typical work function for a solid is about 5 eV, and it is desirable to produce photoelectrons with kinetic energies >5 eV because they are relatively impervious to typical stray electric and magnetic fields and final state effects are minimized. Thus, typical photon energies used for valence band photoemission experiments are in the 10 eV to 40 eV range. Because almost all materials are opaque in this energy range (with LiF having the highest energy transmission cutoff of ~11.6 eV), most systems have no window between the photon source and the sample. Gas discharge lamps are the most popular sources of the intense quasi-monochromatic UV radiation needed for an efficient valence-band photoemission experiment. The lamp contains a small tubular region that is fed with an inert gas. An electrical discharge is struck and tuned so that a single atomic transition dominates the emission from the plasma. The discharge region is separated from the main experimental chamber by a quartz capillary and several stages of differential pumping. Several such sources are commercially available, and the photon energies of some

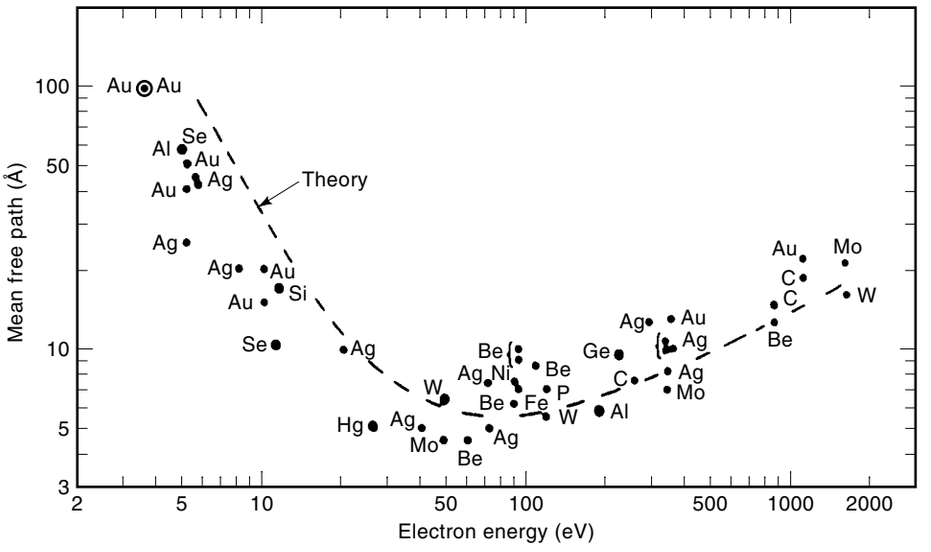

Figure 4. The "universal curve" of electron mean free path versus electron kinetic energy in solids. The points are measurements made on several solids. The dashed curve is a theoretical result. Most photoemission experiments involve electrons with kinetic energies in the 10 eV to 1000 eV range, where the mean free path is less than 10 Å. Therefore, photoemission is a very surface-sensitive probe. From Ref. (2).

commonly used gases are shown in Table 1. The vast majority of valence band photoemission data available to date have been obtained using He-I radiation. Recently, high-resolution photoemission experiments have employed lower-energy photons provided by Hg discharge lamps (3). Such sources often operate below the LiF cutoff and can be isolated from the sample chamber.

The most popular photon source for XPS is the metal X-ray anode source. Once again, this source relies upon the sharp emission lines of atomic transitions for its intense, quasi-monochromatic nature, but in this case the transitions involve the inner shells of the anode material. The anode consists of a metal target, most commonly an Al- or Mg-coated Cu rod, that is held at a high positive potential in the vicinity of a hot filament. Electrons thermionically emitted from the filament are accelerated and bombard the anode ejecting inner shell electrons. Radiative decay of these excited ions produce X-rays at the characteristic shell energies of the atom. Typically the K_α radiation is most intense. X-ray sources are often separated from the experimental chamber by a thin Al foil that serves both to reduce the background of undesired photons and to separate the sample chamber from the anode environment. Occasionally, if high-energy resolution is needed, a monochromator is placed between the X-ray source and the sample.

Table 1. Photon Energies of Resonance Lines

Line	Energy (eV)
He I	21.21
He II	40.82
Ne I	16.85
	16.67
Ne II	26.9
	27.8
	30.5
Ar I	11.83
	11.62
Ar II	13.84
	13.30

By far the most versatile photon source, but also the most complicated to use, is a synchrotron radiation source. Taking advantage of high brightness and continuum nature of synchrotron radiation produced at an electron storage ring, the photon energy gap between discharge lamps and X-ray anodes is easily bridged. In fact, with the latest innovations in insertion devices and monochromators, synchrotron radiation sources can provide photon fluxes that rival laser sources, but over a much broader spectral range and in an energy region all but inaccessible to current laser technology. Synchrotron radiation also offers features that are difficult to include with conventional sources such as a high degree of polarization (both linear and circular) and a pulsed nature that is very convenient for time resolved experiments. The price one must pay for the increased flexibility and capability of a synchrotron source is the added complexity and expense of maintaining the storage ring, as well as the beamlines which transport, disperse, and focus the radiation. Since the photon energy range of interest is from the hard UV to the soft X-ray, beamlines must be evacuated and employ reflection optics operating near glancing incidence to minimize losses. In addition, curved diffractive elements are used to combine focusing and dispersive functions, thereby reducing the number of optical elements.

Once an excitation source is chosen, one must consider energy analysis and detection of the photoemitted electrons. There are only a few modes of collection and analysis that are commonly employed, and they are sketched in Fig. 5. Most analyzers use a combination of (1) electrostatic deflection (which will generate different trajectories for different kinetic energy electrons) and (2) a slit or aperture for energy selection. A most efficient analyzer that is commercially available is the cylindrical mirror analyzer (CMA) shown in Fig. 5(a). This analyzer accepts a cone of width $\pm 12°$ about an average angle of 42.6° from the cylinder axis. As such, it is an angle integrating analyzer used primarily for applications that require high counting efficiency. A drawback of this analyzer is that it has a cylinder diameter of approximately 15 cm and requires rather close sample-to-analyzer distance. As a result, the sample region must be relatively free from other obstruc-

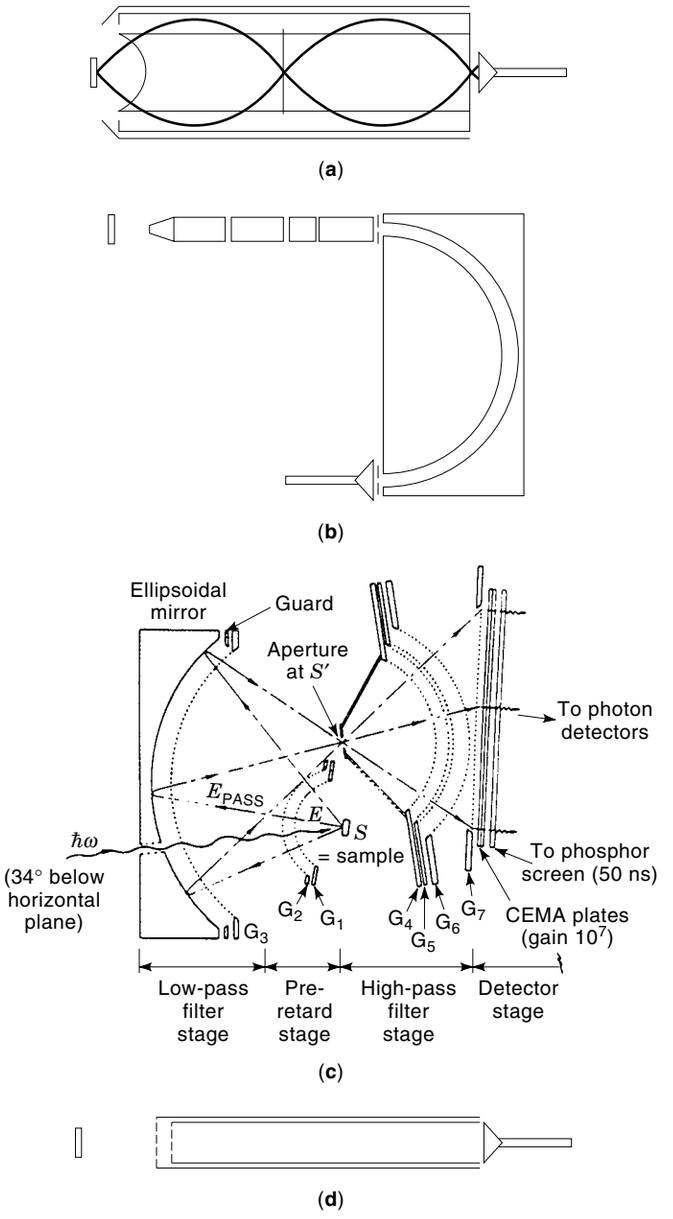

Figure 5. Electron energy analyzers commonly used for photoemission experiments. (a) Cylindrical mirror analyzer (CMA). The CMA consists of two concentric cylinders that are held at different potentials. Electrons generated at the sample pass through grids in the inner cylinder and are deflected by the electric fields between the two electrodes. Electrons that have the desired energy will pass through a second set of grids and a restricting axial aperture. A double-pass CMA is illustrated where the electrons must pass through a second identical arrangement of cylinders before passing through the exit aperture and being detected by a channel electron multiplier (CEM). This analyser integrates over azimuthal angles about its axis of symmetry. (b) Hemispherical analyzer. In this instrument, energy analysis is achieved by deflecting electrons in the gap between two concentric hemispherical electrodes. The electrons are focused on the entrance to the gap by a series of cylindrically symmetric electrostatic lenses. This enables variation of angular, spatial, and energy resolution. Upon exiting the analyzer, electrons may pass through a slit into a CEM, or they may be detected by a microchannel plate followed by a position-sensitive detector. In the latter mode, several electron energies may be simultaneously acquired. (c) Elliptical mirror analyzer (EMA). The electrodes in this instrument possess elliptical symmetry. Photoelectrons emitted by the sample, which is placed at one focus of the ellipse, are deflected by an electrostatic mirror that also acts as a low-pass filter. They pass through an aperture at the second focus and pass through a grid system that acts as a high-pass filter. The electrons that survive this energy band-pass filter are then detected by a multichannel plate and imaged by a position-sensitive detector. This analyzer has an unusually large acceptance angle and provides both energy and angular information about the photoelectrons. From Ref. (4). (d) Time-of-flight (TOF) analyzer. For this technique, photoelectrons from the sample enter a flight tube after passing through several grids that prevent unwanted electric fields. There are often two tubes, as shown, so that the electrons may be either accelerated or decelerated to match the optimum performance of the tube. The electrons are then detected by either a CEM or an MCP. The TOF technique requires a pulsed source as a reference for the timing signal.

tions for effective use. Furthermore, optimal efficiency is obtained if the sample normal is along the cylinder axis. The rather large average angle of the acceptance cone means that significant loss of signal will be encountered if the sample normal is more than ~45° from the CMA axis.

A second very popular analyzer design is the concentric hemispherical analyzer. A sketch of such an analyzer is shown in Fig. 5(b). Typically, such an analyzer will have a set of electron optics on the entrance end of the device so that electrons emitted from the sample with a certain acceptance cone can be properly focused and decelerated for optimal energy resolution and transmission through the analyzer. There are several important advantages to this analyzer. The entrance optics is often rather compact and removed from the analyzing hemispheres. Therefore one can access a sample more easily than with a CMA. Furthermore, the input optics can allow for adjustment of the acceptance conditions. With an appropriate lens design, the angular acceptance, as well as energy resolution of the analyzer, may be independently adjusted to the specific application. Finally, it is possible to remove the exit aperture at the exit plane of the hemisphere to allow parallel energy detection with a position-sensitive detector.

A third type of analyzer that has been gaining in popularity in recent years is the ellipsoidal mirror analyzer of Fig. 5(c) (4). In this approach, the sample is placed at one focus of an ellipsoidal electron mirror, and an aperture is placed at the second focus. Photoelectrons emitted from the sample with kinetic energy less than the mirror bias will be reflected refocused to the aperture. As such, this leg of the analyzer acts as a low-pass filter. After the aperture, a retarding grid system is used as a high-pass filter so that the combination acts as a band-pass filter and provides the energy-resolving capabilities of the analyzer. After the exit grids, the electrons are detected on a position-sensitive detector. There are two primary advantages to this approach. First, since the analyzer captures a large solid angle around the sample, it is extremely efficient. Moreover, since the angles are maintained throughout the analyzer, the position of the electron emission on the detector corresponds directly to an emission angle from the sample. Therefore, one can perform angle-resolved photoemission measurements by simultaneously acquiring a large range of emission angles. The principal draw-

backs of this analyzer are that it is a complicated and delicate instrument so mechanical stability is critical. Furthermore, the sample is in a very confined region during data acquisition, and there are often considerable distortions throughout the optical system. Nevertheless, this type of analyzer is becoming particularly popular for performing photoelectron diffraction experiments (see below) where variation in the intensity of photoemission signal as a function of either polar or azimuthal angle is related to the atomic arrangement of the sample surface.

There are a number of other electron energy analysis and detection schemes that are currently used in research situations, but none is as widely employed as those discussed above. Nevertheless, time-of-flight (TOF) energy analysis deserves some mention since it finds application in other spectroscopic techniques as well. The technique is based on the principle that it takes different time periods for electrons emitted with different kinetic energies to follow the same path to the detector. As shown in Fig. 5(d), electrons exiting the sample traverse a field-free region before encountering an accelerating field between two grids. The electrons then enter a field-free drift tube providing sufficient flight time to give the desired energy resolution. By measuring this time period, the kinetic energy spectrum of photoemitted electrons can be determined. Clearly, this technique is tailored for pulsed sources such as synchrotrons or laser sources. Ultimately, the energy resolution depends upon the duration of the photon pulse compared to the analysis time.

ELEMENTARY PRINCIPLES OF PHOTOEMISSION

In the section entitled "The Basic Properties of the Photoemission Spectrum," the energetic considerations of the photoexcitation process and the interpretation of the spectrum in terms of the independent electron approximation were discussed. Here we will describe what is known as the three-step model of photoemission, where the photoemission process is divided into photoexcitation, transport to the surface, and emission. Photoexcitation is taken to be a direct transition within the dipole approximation. During transport to the surface, elastic and inelastic scattering processes may occur, the latter being the primary source of secondary electrons. Finally, emission from the surface influences the conservation rules that relate the kinetic energy and momentum of the detected electron to those of the photoelectron prior to excitation.

The Hamiltonian obeyed by the electrons in a solid may be written as

$$H_0 = \left(\frac{1}{2m}\right)\boldsymbol{p}\cdot\boldsymbol{p} + V(\boldsymbol{r}) \tag{5}$$

where $\boldsymbol{p}$ is the momentum operator and $V(\boldsymbol{r})$ is the electrostatic potential, including interactions with both the ions and the other electrons in the system. In the presence of an electromagnetic field, the Hamiltonian is modified to the following form:

$$\begin{aligned} H &= \frac{1}{2m}\left(\boldsymbol{p} - \frac{e}{c}\boldsymbol{A}(\boldsymbol{r},t)\right)^2 + e\phi(\boldsymbol{r},t) + V(\boldsymbol{r}) \\ &= H_0 + H_{\text{int}} \end{aligned} \tag{6}$$

where

$$H_{\text{int}} = \frac{e^2}{2mc^2}\boldsymbol{A}^2 - \frac{e}{2mc}(\boldsymbol{A}\cdot\boldsymbol{p} + \boldsymbol{p}\cdot\boldsymbol{A}) + e\phi$$

We can choose a gauge where the $\phi = 0$, and usually the term in $\boldsymbol{A}^2$ is small and can be neglected. From the commutation relation $\boldsymbol{A}\cdot\boldsymbol{p} - \boldsymbol{p}\cdot\boldsymbol{A} = -i\hbar\,\nabla\cdot\boldsymbol{A}$, we can solve for $\boldsymbol{p}\cdot\boldsymbol{A}$. Furthermore, since the wavelength of the photons is much larger than atomic dimensions, $\nabla\cdot\boldsymbol{A}$ is negligible. Combining these results, the form of the interaction Hamiltonian is simplified to

$$H_{\text{int}} = \left(\frac{e}{mc}\right)\boldsymbol{A}\cdot\boldsymbol{p} \tag{7}$$

Considering this as a perturbation, the transition rate for photoexcitation obtained from Fermi's Golden Rule is given by

$$\Gamma \propto \frac{2\pi}{\hbar}|\langle\psi_f| - \left(\frac{e}{mc}\right)\boldsymbol{A}\cdot\boldsymbol{p}|\psi_i\rangle|^2\delta(E_{\text{f}} - E_{\text{i}} - \hbar\omega) \tag{8}$$

Since the wavelength of the electromagnetic field is large compared to a unit cell of the crystal, we neglect the spatial dependence of $\boldsymbol{A}$ in the matrix element and write

$$\Gamma \propto \frac{2\pi}{\hbar}\left|\left(\frac{-e}{mc}\right)\boldsymbol{A}\cdot\langle\psi_{\text{f}}|\,\boldsymbol{p}|\psi_{\text{i}}\rangle\right|^2\delta(E_{\text{f}} - E_{\text{i}} - \hbar\omega) \tag{9}$$

This is the dipole approximation to the photoexcitation rate. Up to this point, we have not specified the wave functions that enter this equation. In principle, the full many-body wave functions should be used for the initial and final states. In practice, however, it is usually both useful and sufficiently accurate to use the single-particle states of the solid as the initial state and use a free electron as the final state. That is, we use atomic wave functions to approximate the core levels and Bloch states for the valence band.

Equation (9) indicates that within the three-step model, photoexcitation from the valance band can be viewed as a direct optical transition between the bands of the solid. This notion is illustrated in Fig. 6. The initial state is some occupied level of the valence band, while the final state is an unoccupied state that is separated in energy from the initial state by the photon energy. For typical energies ($\lesssim$1000 eV), the momentum of the photon is negligible compared to that of the electron and is ignored. Conservation of momentum then dictates that the initial and final states have the same momentum in the reduced zone scheme, and the excitation is represented by a vertical transition in the band structure. In general, the momentum of the photoexcited electron has components parallel and perpendicular to the surface. The angle of emission is therefore related to the momentum of the electron within the solid. We will discuss this point in detail when we address angle-resolved photoemission below.

If we return to Eq. (9), we can derive an expression for $N(E, \hbar\omega)$, the total number of photoelectrons emitted at en-

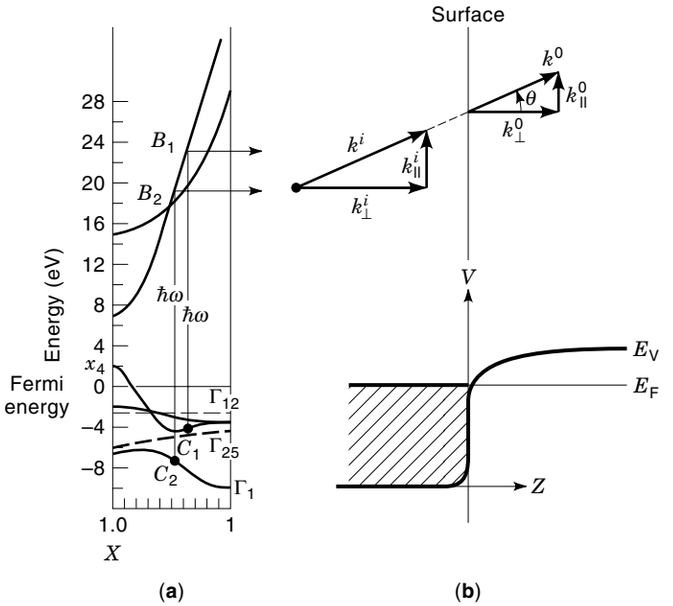

Figure 6. (a) The relationship between photoemission and the band structure of a hypothetical solid. Photoexcitation in a crystalline solid may be viewed as a direct transition of an electron from a filled band to an empty band in the reduced zone scheme. (b) Crystal momentum of a photoexcited electron both inside and outside the solid, along with a schematic diagram of the crystal potential near the surface. After excitation, the photoelectron must propagate to the surface. Inside the solid it has a definite crystal momentum, k^{i}. As translational symmetry parallel to the surface is maintained, $k_{\parallel}$ is conserved upon emission so $k^0_{\parallel} = k_{\parallel}$. The lack of translational symmetry normal to the surface implies that $k_{\perp}$ is not conserved in the photoemission process.

ergy E (with respect to the Fermi level) after excitation with photon of energy $\hbar\omega$. This quantity is given by

$$N(E, \hbar\omega) \propto \sum_{ij} \int |\boldsymbol{A} \cdot \langle \psi_{\mathrm{f}} | \boldsymbol{p} | \psi_{\mathrm{i}} \rangle|^2 \delta(E_{\mathrm{f}}(k) - E_{\mathrm{i}}(k) - \hbar\omega) \delta(E_{\mathrm{f}}(k) - E)\, d^3k \quad (10)$$

or equivalently

$$N(E, \hbar\omega) \propto \sum_{ij} \int |M_{\mathrm{fi}}|^2 \delta(E_{\mathrm{f}}(k) - E_{\mathrm{i}}(k) - \hbar\omega) \delta(E_{\mathrm{f}}(k) - E)\, d^3k \quad (11)$$

where M_{fi} is known as the dipole matrix element. In principle, M_{fi} is complicated and depends upon the momentum of the electrons participating in the transition. Often, however, it is sufficient to assume that the matrix element is independent of k, that is,

$$M_{\mathrm{fi}} \neq M_{\mathrm{fi}}(k) \quad (12)$$

Furthermore, it is usually sufficient to assume that the final states are well-described by a free-electron-like dispersion. That is, the final state energy depends only on the square of the magnitude of the $\boldsymbol{k}$ vector:

$$E_{\mathrm{f}}(\boldsymbol{k}) = E_{\mathrm{f}}(k) = \frac{\hbar^2 k^2}{2m^*} \quad (13)$$

where the presence of the lattice potential is accounted for by the inclusion of an effective mass, m^*. With these assumptions, we have

$$N(E, \hbar\omega) \propto \sum_{ij} |M_{\mathrm{fi}}|^2 \mathscr{D}(E - \hbar\omega) \quad (14)$$

where

$$\mathscr{D}(E - \hbar\omega)$$

is the density of states (DOS) of the solid at energy $(E - \hbar\omega)$. Finally, neglecting the energy dependence of the matrix elements, and recognizing through energy conservation that $E - \hbar\omega = E_{\mathrm{i}}$, we see that

$$N(E, \hbar\omega) \propto \mathscr{D}(E_i) \quad (15)$$

In other words, the kinetic energy distribution of the photoemission spectrum reflects the density of states in the solid. Much of the time, this is a rather good approximation, as illustrated in Figs. 7(a), 7(b), and 7(c) (5). Here for the noble metals we see that the experimental spectrum agrees quite well with theoretical predictions of the valence-band DOS. On the other hand, as seen for the Ni spectrum in Fig. 7(d) (5), this approximation is not always successful. Here, one sees extra structure, particularly an extra peak at ~6 eV binding energy, for which there is no corresponding feature in the Ni DOS. In this particular case, this additional feature is caused by excitation effects and serves as a reminder that photoemission spectra do not reflect the ground-state properties of the system.

After photoexcitation, one must consider the electron's propagation to, and emission from, the surface. Typically, UV and X-ray photons penetrate several tens or hundreds of nanometers into the solid. Therefore, photoexcitation may occur far from the surface. Owing to the short MFP, the main consideration regarding propagation to the surface is the possibility for inelastic collisions with other electrons in the solid. Inelastic scattering has two effects. First, it limits the escape depth of primary photoelectrons. The probability of escaping the solid without suffering and inelastic collision goes as

$$P(x) = e^{-x/\lambda} \quad (16)$$

where x is the depth beneath the surface that the photoelectron was created, and λ is the inelastic mean free path. With $\lambda \lesssim 1$ nm, most of the photoemission signal comes from the first or second layer of the sample. Furthermore, this expression enables one to determine the concentration and depth profile of species in a system either by comparison to known standards or by comparison to other components in the system.

The second result of the short MFP is that many photoelectrons generated deep in the sample lose some energy but still are able to escape from the sample. These electrons are the main contribution to the secondary electron background illustrated in Fig. 1. The exact shape of this background is difficult to determine owing to the large array of possible scattering events that may occur. However, a very useful and physically reasonable approximation has been developed by Shirley (6), where the background at a given kinetic energy is propor-

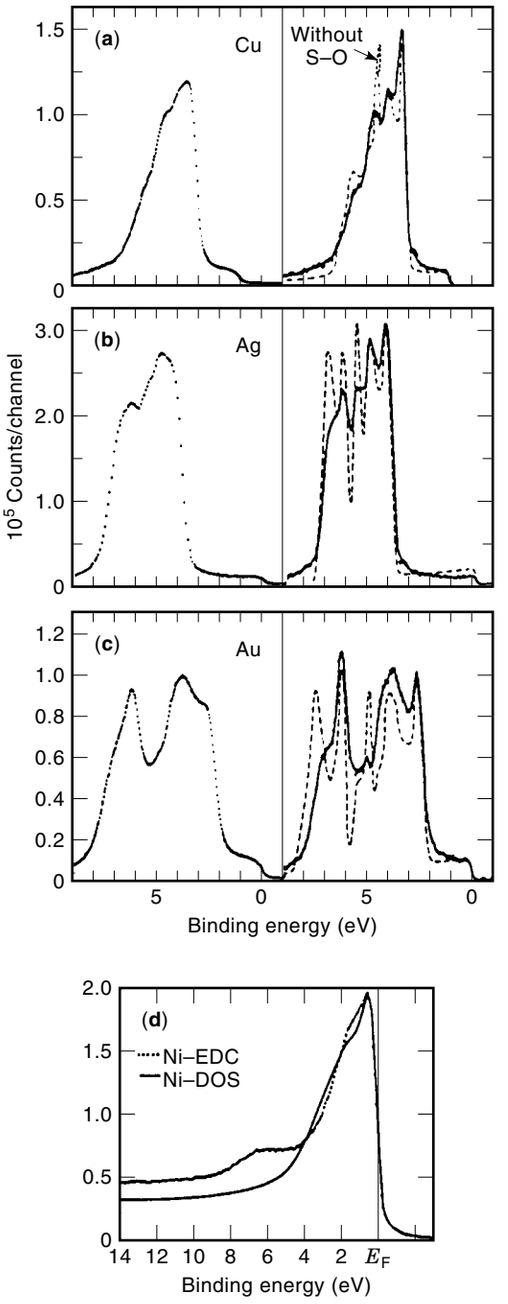

Figure 7. Angle-integrated photoemission spectra (left panel) and density of states calculations (right panel) from (a) Cu, (b) Ag, (c) Au, and (d) Ni. Good agreement between experiment and theory is seen for the noble metals. For Ni, a feature near 6 eV, associated with different screening states, appears in the photoemission spectrum but is absent in the calculation. From Ref. (5).

tional to the integrated intensity of all primary electrons at higher energy, and more recently using a more extensive consideration of energy loss mechanisms by Tougaard (7). The intensity of the secondary electron background increases at low kinetic energies, indicating that it is advantageous to increase the kinetic energy of the photoelectron to minimize this contribution.

The last stage of the three-step model is emission from the surface. The most important aspect of this step is its influence on the momentum of the photoelectron. A truncated single crystal is periodic in translations by a lattice vector parallel to the surface, but is not periodic perpendicular to the surface. As a result, momentum parallel to the surface is conserved up to a surface reciprocal lattice vector, while perpendicular momentum is not conserved. This means that the component of the photoemitted electron's wave vector parallel to the surface is the same as its wave vector prior to emission, $\boldsymbol{k}_{\parallel}^{0} = \boldsymbol{k}_{\parallel}^{i}$. In contrast, the perpendicular momentum of the detected photoelectron cannot be readily associated with the electron momentum in the solid. These effects have important consequences in the context of angle-resolved photoemission and will be discussed in more detail below.

As a final note in this section, we point out that one must remain cautious because, while legitimate much of the time, the assumptions and approximations cited above may not always be valid. We have already encountered an example of excitation effects influencing the valence-band photoemission spectrum of Ni. Similarly, for $\hbar\omega$ near the plasmon energy, $\nabla \cdot \boldsymbol{A}$ is not small and dramatically affects photoemission cross sections. Furthermore, M_{fi} is not truly independent of energy and momentum. In fact, one can take advantage of this fact to help identify the orbital character of features in the spectrum. These points notwithstanding, the description given here is a good starting point for the interpretation and analysis of photoemission spectra.

APPLICATIONS OF PHOTOEMISSION

A wealth of information about the material under consideration, as well as photoexcitation and decay processes, is revealed in the photoemission spectrum. In this section, we will describe some of the most basic information that is contained in the photoemission spectrum. We divide the discussion into five sections, each dealing with a primary application of the technique.

Core-Level Photoemission

We will focus on the two properties of core-level features in photoemission spectra: energy position and intensity. In principle, core level line shapes are given by what is known as a Doniach-Sunjic line shape (8). This is essentially a Lorentzian line shape, associated with the life time of the core hole, distorted with increased intensity at low kinetic energies by the possibility of low energy electron-hole pair excitations. In many cases, however, poor instrumental resolution obscures this phenomenon and the experimental line shape can be approximated by a Gaussian.

Core-level photoemission spectra from Ta(100) (9,10) and Si(100) (11) excited by synchroton radiation are shown in Fig. 8. Figure 8(a) shows how the core levels are pronounced features in a wide energy scan. The most common use of core-level photoemission is for elemental identification. As the binding energy of a particular core level is specific to that species, the technique can be easily employed to determine the composition of the surface region of the sample. Furthermore, as the relative photoemission cross sections for different levels of each element are well known, one can estimate the composition depth profile of a sample. It is also possible to

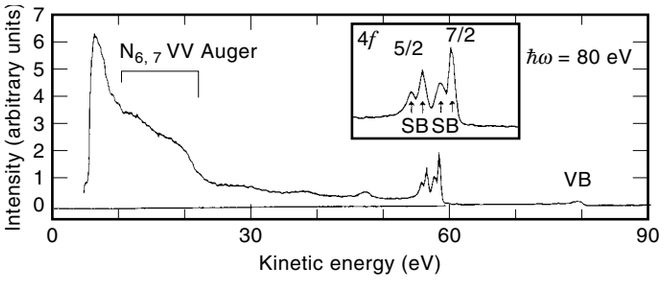

(a)

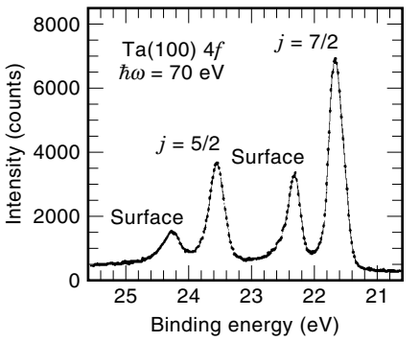

(b)

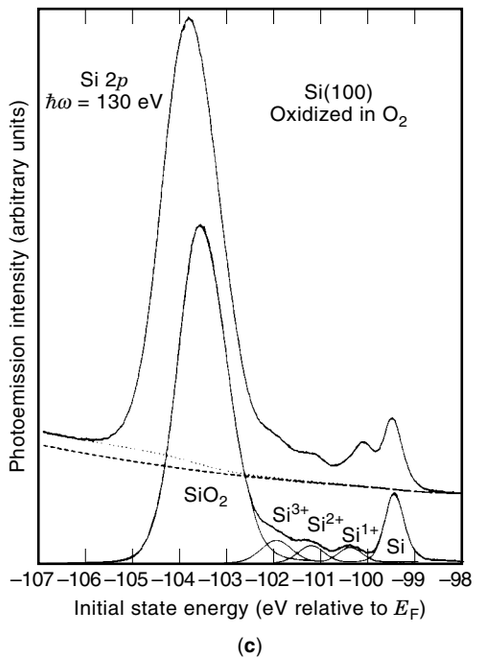

(c)

Figure 8. Photoemission spectra containing the core levels of Ta and Si. (a) A wide scan photoemission spectrum from Ta(100) obtained at $\hbar\omega = 80$ eV. Note that the Ta 4*f* levels exhibit four sharp peaks. From Ref. (9). (b) A close-up scan of the Ta 4*f* levels illustrating that the $4f_{7/5}$ and $4f_{5/2}$ members of the spin–orbit split doublet each has a well-resolved surface-shifted component. From Ref. (10). (c) The Si 2*p* core level from Si(100) after the surface has been exposed to oxygen. The upper curve is the raw data which contains contributions from both the Si $2p_{1/2}$ and $2p_{3/2}$ core levels. In the lower curve, the $2p_{1/2}$ contribution has been removed and the remaining curve fit to different Si oxidation states illustrating substoichiometric regions at the oxide–semiconductor interface. From Ref. (11).

monitor core-level intensities as a function of some processing parameter, such as gas dosage or metal overlayer thickness, so that the compositional or morphological properties of the surface may be determined.

Well-ordered samples often exhibit a surface core-level shift. This shift occurs even in elemental solids and is the result of a difference in potential at a surface atom as compared to bulk atoms. For the narrow and well-separated 4*f* levels of Ta(100) in Fig. 8(b), the surface-shifted core levels are easily observed. Surface core-level shifts have been observed on many metals and semiconductors and have been very useful in determining the structure and chemical interactions with surfaces.

Another important use of core-level photoemission is to assess the bonding properties at the sample surface. Although they do not participate directly in the chemical bonding process, the binding energy of core electron is influenced by its environment. For example, when oxidized, metal atoms tend to donate charge to the oxygen atoms to which they are chemically bonded. As a result, the core electrons of the metal are less efficiently screened from the nucleus, and the additional Coulomb attraction leads to an increase in binding energy. This is illustrated in Fig. 8(c), where the core levels for Si in different oxidation states can be clearly resolved.

The intensity of core levels in photoemission spectra depend upon several factors. For a particular core level, the cross section as a function of photon energy is typically characteristic of its orbital angular momentum quantum number. For example, the 3*d* levels of Ag and the 4*d* levels of Au exhibit very similar photon-energy-dependent cross-section variations when the differences in binding energies is taken into account. On the other hand, the profile differs greatly from the 3*p* level of either. Moreover, the cross section often is a nonmonotonic function of energy, and it may exhibit several local maxima. One of the most interesting phenomena causing such behavior is called resonant photoemission and will be discussed in the next section.

Valence-Band Photoemission

Valence-band photoemission is typically conducted using the He-I or He-II UV radiation from a resonance discharge lamp. In an angle-integrated mode, the spectrum can provide some very basic information, such as (1) revealing the presence of electron density at the Fermi level or (2) the presence of electron charge of different orbital character. For example, the intense emission ~3 eV below the Fermi level in the Cu photoemission spectrum of Fig. 7(a) is caused by the Cu 3*d* band, as opposed to the weak emission near the Fermi level that is associated with the lower electron density of the *sp* band.

One of the most important uses of photoemission is to characterize changes in the electronic structure of a solid or surface upon a controlled modification, such as the adsorption of small molecules. Figure 9(a) (12) shows the UPS spectrum from Ni obtained before and after adsorption of benzene at room temperature. The most obvious changes in the spectrum are (1) a reduced intensity in the region of the Ni *d* bands and (2) the addition of four new peaks at binding energies greater than 4 eV. By comparison to the gas-phase photoemission spectrum of molecular benzene, one can conclude that the adsorbate remains intact on the surface, and the energy shift of the highest energy π level indicates its participation

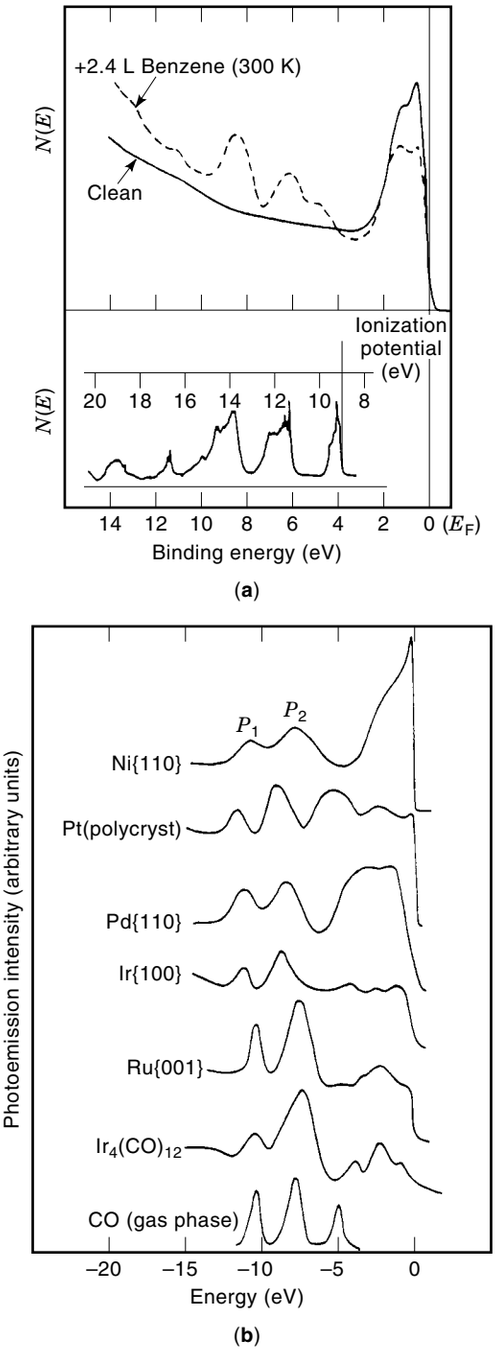

Figure 9. Angle-integrated photoemission spectra from molecules adsorbed on several transition metal surfaces. (a) (upper panel) Clean and benzene-covered Ni(100) surface. The peaks between 4 eV and 15 eV binding energy are from adsorbate orbitals. By comparison with the photoemission spectrum of benzene in the gas phase (lower panel), identification of the adsorbate states can be made. Note that the orbitals closest to the Fermi level are shifted owing to the bonding process. From Ref. (12). (b) Photoemission spectra from CO adsorbed on several transition metal surfaces. On different surfaces, the CO orbitals are shifted by different amounts. Note that all spectra show two adsorbate-induced peaks rather than the three that are seen in the gas-phase spectrum (lower curve). This is because of a bonding shift of the 5σ orbital to lower energy so that is nearly degenerate with the 1π level. From Ref. (13).

in the bonding. This sort of fingerprinting of adsorbates is a common use of photoemission, and a survey of CO adsorption on several transition metals is shown in Fig. 9(c) (13). Once again, the highest energy 5σ level of the CO molecule is shifted down in energy, by different amounts for different substrates, indicating its role in bonding of the molecule to the surface.

The valence band of many compound solids contain contributions from several orbitals, perhaps even from different species. Often, it is possible to use the cross-section variations as a function of excitation energy to distinguish orbital character or detect hybridization among the constituent elements. An important example of this is the resonant photoemission process where the quantum mechanical interference between two excitation channels, one of which has a well-defined excitation energy, causes dramatic intensity modulations. The phenomenon is nicely illustrated in the UPS spectra from $Ti_2O_3(10\bar{1}2)$ shown in Fig. 10 (14). Identification of the weak emission near the Fermi level seen in the 30 eV spectrum as occupied Ti $3d$ levels was verified by its excitation energy dependence. As can be seen in the figure, this feature exhibits strong resonant behavior as the photon energy crosses the Ti $3p \rightarrow 3d$ optical absorption threshold near $\hbar\omega = 46$ eV. It is interesting to note that the nominal O $2p$ band also shows resonance effects indicating hybridization with the Ti $3d$ levels.

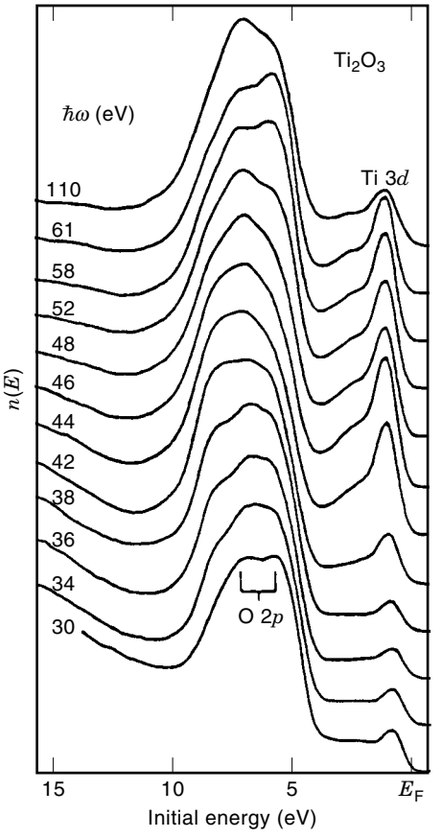

Figure 10. Resonant photoemission spectra from $Ti_2O_3(10\bar{1}0)$. Note how the intensity of the Ti $3d$ levels near the Fermi level undergo strong intensity oscillations as the photon intensity is increased. From Ref. (14).

Angle-Resolved Photoemission

Equation (10) gave an expression for the number of photoelectrons emitted as a function of energy without regard to the angle of emission. Furthermore, it was pointed out that photoexcitation in the solid is an energy- and momentum-conserving process, and it was noted that momentum information is preserved for those electrons that do not suffer inelastic scattering. Furthermore, upon emission from the surface, $k_\parallel$ is also conserved. Therefore, by measuring the energy and emission angle of a photoelectron we can determine its parallel momentum prior to emission, which in turn is directly related to the parallel momentum of the electron prior to excitation.

When the photoelectron has escaped the solid, it may be treated as a free electron. Therefore, the magnitude of its wave vector is simply related to its energy by the expression

$$E = \frac{\hbar^2 k^2}{2m} \tag{17}$$

where E is the kinetic energy of the electron. As is illustrated in Fig. 6, the magnitude component of the wave vector parallel to the surface is given by

$$k_\parallel = k \sin(\theta) \tag{18}$$

where θ is the angle of emission measured with respect to the surface normal. Combining Eqs. (17) and (18) we find an expression for $k_\parallel$ in terms of experimentally measurable quantities:

$$k_\parallel = \frac{\sqrt{2mE}}{\hbar} \sin(\theta) \tag{19}$$

The implications of measuring the parallel momentum of the photoelectron is suggested by Eq. (10). Rather than measuring the density of states, one can now associate the peaks in an angle-resolved photoemission spectrum to direct transitions between energy levels of the solid, as illustrated in Fig. 6. Since the parallel momentum of the detected photoelectron is the same as that of the final state, and the direct transition satisfies momentum conservation, the parallel momentum of the initial state is directly determined. On the other hand, the perpendicular momentum is not known *a priori.* However, since the energy of the photoexcited electron is typically several tens of electronvolts, the final states are well-described by a free-electron-like dispersion, perhaps with an effective mass. Using this procedure, the final energy can be associated with a perpendicular momentum, and thus the momentum of the initial state energy is determined.

Employing a variable photon energy source, one can use angle-resolved photoemission to map the valence bands of a solid. The simplest procedure is to consider electron emission normal to the surface—that is, for $k_\parallel = 0$. Under these conditions, changes in the kinetic energy of a photoemission feature represents changes in perpendicular momentum only. Using free electron final states, the valence band of GaAs along the (100) or ΓX direction of the bulk Brillouin zone have been experimentally determined (15) and compared to theoretical calculations (16). The level of agreement between theory and experiment seen in Fig. 11 shows that angle-resolved photoemission data can provide a rigorous test of our understanding of electronic structure of solids.

Recently, high-resolution angle-resolved photoemission has become one of the most important tools for understanding and exploring the Fermi level properties of several important new materials such as the high-temperature superconductors and the colossal magnetoresistance materials (17). The location in the surface Brillouin zone where different states cross the Fermi level has been key evidence for d-like symmetry for the superconducting order parameter in these systems. However, these systems exhibit a complicated lineshape in the region of the Fermi level, and interpretation of the spectra are in part dependent upon how this background is treated. To better understand these effects, there has been considerable effort concentrated on high-resolution photoemission spectra of surface states on metals.

In contrast to valence-band photoemission, the angular distribution of core-level photoelectrons is understood in terms of photoelectron diffraction. Here, angular effects result from the transport of the photoexcited electron to the surface. Part of the excited electron's wave function propagates directly to the detector, while other parts scatter from neighboring atoms. The direct and scattered waves recombine, producing diffraction effects that influence the photoemission intensity as a function of both excitation energy and emission angle. A relatively simple analysis of the form factor for the scattered wave shows that for electron kinetic energies $\gtrsim$500 eV, the intensity distribution is strongly peaked in the forward scattering direction. This means that for an emitter atom below the surface, the photoemission intensity is peaked along the bonding direction to nearest neighbors. This so-called forward-focusing effect is very useful in determining the geometric structure of adsorbates or overlayers. Moreover, since the core levels under investigation may undergo chemical shifts, it is possible to independently determine the geometric structure of atoms of the same system that are in different chemical states. Symmetry determinations, such as whether an overlayer has face-centered cubic (fcc) or body-centered cubic (bcc) structure, can be most easily determined. Typically, bond length determination is more difficult and has an accuracy of order 0.05 Å. There has been considerable effort devoted to taking photoelectron diffraction to its ultimate limit: photoelectron holography. This analysis exploits coherence between the emitted and scattered waves in order to produce a real-space holographic image of the atomic geometry around the emitter atom. Very promising results have been obtained from some systems with known atomic geometries. The application of this technique to new systems is a very active topic of current research.

Magnetic Measurements with Spin Analysis of Photoelectrons

Many transition metals exhibit magnetic behavior owing to a strong exchange interaction of the itinerant electrons in the valence band. In addition, theoretical calculations have predicted that magnetism should be enhanced at surfaces or for thin films owing to the reduced dimensionality. These important effects can be observed and analyzed by resolving the spin state of the photoemitted electrons. This is a technically demanding experiment where the efficiency of spin detectors

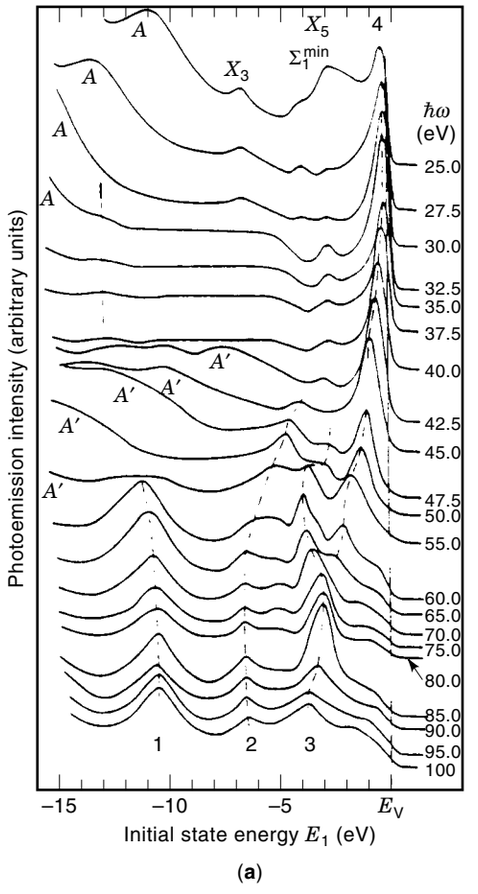

(**a**)

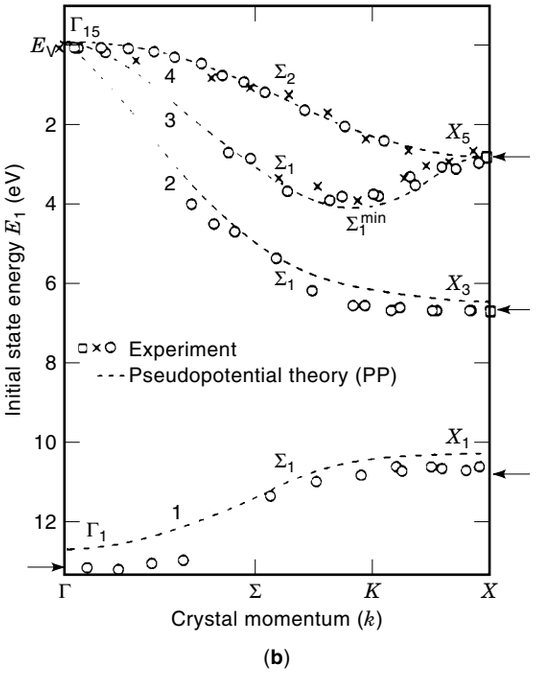

(**b**)

Figure 11. (a) Angle-resolved photoemission spectra from GaAs(110) at normal emission. The spectra are shifted by the photon energy so that emission from the Fermi level is aligned in each case. The peaks in the spectra are associated with direct transitions of the type described in Fig. 6. Note that the peaks change binding energy with different photon energies. (b) Dispersion plot of energy versus perpendicular momentum for the peaks in the photoemission spectra of (a). From Ref. (15). The dashed lines show the calculated dispersions along the direction probed by the spectra in (a). Note the excellent agreement between theory (16) and experiment.

is typically in the 10^{-3} to 10^{-5} range. As a result, most spin-polarized photoemission experiments are performed using a synchrotron radiation source.

Spin-polarized photoemission can allow very direct measurement of the exchange splitting in the valence band. This is illustrated quite dramatically in Fig. 12(a) (18) where different symmetry points of the majority and minority spin band structure are identified in the spin-up and spin-down photoemission spectra of Fe(001). Owing to the spin–orbit interaction, nonmagnetic samples also exhibit spin-dependent effects in photoemission. An interesting example is shown in Fig. 12(b) (19), where the W 4*f* levels show dramatic and complementary spin-dependent spectra when excited with left- or right-handed circularly polarized light.

One of the most interesting recent developments in magnetic materials is the observation of the giant magnetoresistance (GMR) effect in metallic multilayers with ferromagnetic (FM) films separated by nonmagnetic (NM) spacer layers. In the NM layer, the electronic states near the Fermi level are largely confined to the layer by quantum size effects, and spin-polarization of these states owing to scattering from the FM layer has been suggested. Both conventional and spin-polarized photoemission spectra from the Ag/Fe(100) metallic quantum well (MQW) system are shown in Fig. 13 (20). The strong feature at about 2 eV binding energy in the spin-integrated spectrum is the Ag-MQW state. It is clear from the spin-polarized spectra that this state has indeed become spin-polarized, and it has minority polarization owing to gap in the minority states of Fe. Studies such as these are having a major impact on our understanding of the magnetic properties of nanoscale systems.

Inverse Photoemission Spectroscopy

The previous sections indicated how photoemission can be used to investigate the occupied electronic states of a solid. For example, angle-resolved, ultraviolet photoemission enables one to map the valance band. However, it is well known that the physical properties of materials depend strongly on the nature of both the occupied and unoccupied states. In particular, the empty states near the Fermi level, such as the conduction band minimum, band gap states, and minority spin states, play key roles in determining the electrical, magnetic, and chemical properties of the solid. The technique of inverse photoemission provides a means of investigating these states, particularly the states between the Fermi level and the vacuum level.

As the name implies, inverse photoemission can to a good approximation be considered as the time-reversed process of photoemission. As illustrated in Fig. 14, the technique involves bombarding the sample with a well-collimated beam of monochromatic low-energy electrons, typically 5 eV $< E_p <$ 25 eV. A small fraction of these electrons will decay radiatively, emitting a UV photon. A spectrum can be obtained in two modes. In the isochromat mode, photons of a fixed energy are collected as a function of incident electron energy. Al-

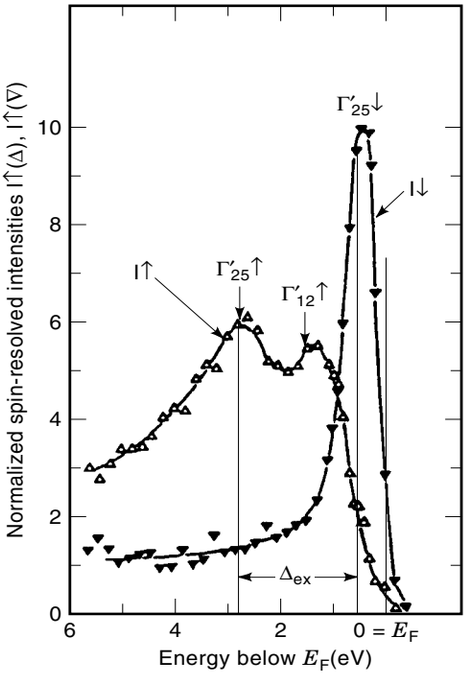

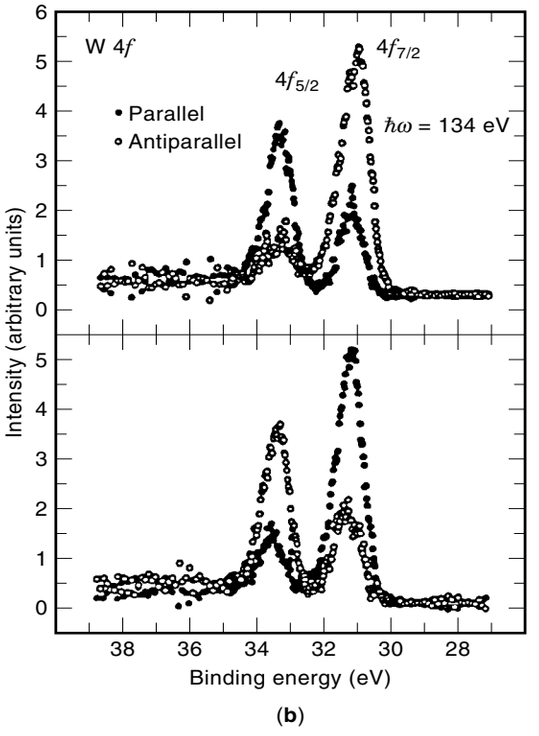

Figure 12. Angle-integrated spin-polarized photoemission spectra. (a) Spectra from the valence band of Fe(001). The upward-pointing triangles probe the majority states, and the downward pointing triangles probe the minority states. Note the strong minority feature near the Fermi level that can be unambiguously identified using spin-polarized photoemission. $\hbar\omega$ = 60 eV. From Ref. (18). (b) Spectra from the W 4*f* levels using circularly polarized light. Note the symmetric change of intensity between the spin-up and spin-down contributions to the $4f_{7/2}$ and $4f_{5/2}$ peaks when the light is changed from left circularly polarized (top) to right circularly polarized (bottom). From Ref. (19).

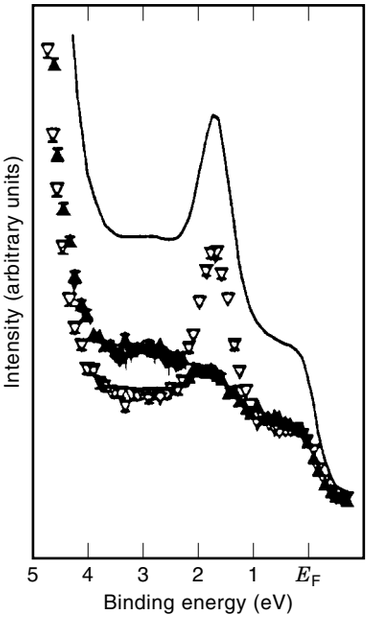

Figure 13. Angle-resolved spin-polarized photoemission spectra from metallic quantum well states of the Ag/Fe(100) system. The solid curve is the spin-integrated spectrum. The sharp feature at 1.8 eV binding energy is a metallic quantum well state in the Ag overlayer. Note that the spin-polarized spectra indicate that this feature is almost exclusively of minority spin character, and that there is some related emission of majority character that is very difficult to uniquely identify in the conventional spectrum. From Ref. (20).

though this approach is relatively easy to implement, it is limited in the information it provides. A more versatile approach is to fix the incident electron energy and disperse and detect the radiation emitted from the sample. As such, photon energy spectra can be obtained for different excitation energies, and it enables one to vary essentially all of the parameters that synchrotron radiation enables for photoemission.

Inverse photoemission in the UV range was first demonstrated by Dose and collaborators in the early 1980s (21) using the isochromat mode. One aspect of IPE that was recognized very early in its history is that the cross section for inverse photoemission is $\sim 10^{-4}$ smaller than that of a photoemission transition in the same energy range. In practical terms, this means that inverse photoemission spectrometers should accept as much radiation from the sample as possible. Higher efficiency such as this is not an issue for the isochromat spectrometers that use Geiger–Mueller tubes. However, for grating spectrographs, the use of faster (low *f*-number) optics comes at the expense of greater aberrations. Because it is relatively easy to produce a well-collimated beam of electrons in the desired energy range, inverse photoemission is almost exclusively conducted in the angle-resolved mode.

Figure 15 (22) shows a series of inverse photoemission spectra from the Cu(111) surface as a function of incident electron angle. The spectrum near normal incidence is dominated by a single peak about 4.25 eV above the Fermi level. This feature corresponds to the image potential state of the surface. When the incident electron approaches the surface, it is attracted by the positive image charge it induced in the metal. If the substrate has a projected band gap in the region of the vacuum level, then the electron can lose energy by

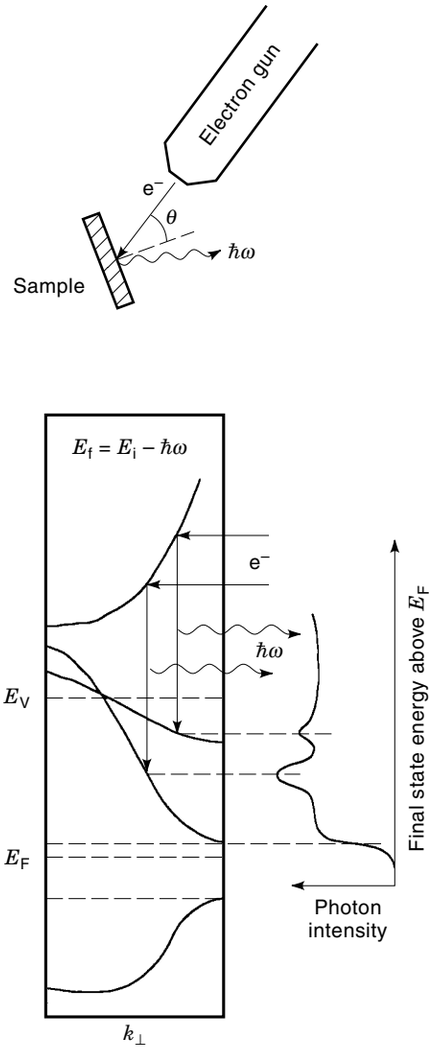

Figure 14. (a) The experimental configuration for inverse photoemission. A well-colimated beam of monochromatic electrons is incident on the sample with an angle θ with respect to the surface normal. Some electrons decay and emit photons that are energy dispersed and detected, or detected using an instrument sensitive to only one photon energy. (b) Schematic diagram indicating the interpretation of inverse photoemission spectra. Analogous to Fig. 6, incident electrons couple to high-lying unoccupied states. A fraction of these electrons will make transition to low-lying empty states and emit a photon. The diagram illustrates the isochromat mode where a single-photon energy is detected while a monoenergetic beam of electrons is swept in energy. The peaks in the spectrum are related to direct transitions and are interpreted in terms of the unoccupied bands of the solid.

emitting a photon and become bound between the surface potential and the repulsive potential of the crystal. A detailed analysis of the image state can give considerable information regarding the nature of the surface potential barrier. Furthermore, as the wave function of the image state is peaked well outside the surface, the state is long-lived has been used as a laboratory for examining electron dynamics at surfaces. Other features in these IPE spectra are well-described by direct transitions between unoccupied states of Cu.

Probing the magnetic properties of the unoccupied states near E_F is a powerful capability of spin-polarized IPE. In Fig. 16 (23), conventional and spin-resolved IPE spectra for N(110) are shown. The conventional spectra show a strong peak at ~0.25 eV above E_F originating from Ni 3*d* levels of minority spin. In the spin-resolved spectra of the second and third panels, it is clearly demonstrated that this feature has essentially 100% minority character. By measurements such as these, the spin-dependent band structure of the unoccupied states can be mapped.

As a final illustration, we discuss the TiO_2(110) surface where the highly complementary nature of direct and inverse photoemission is very evident. TiO_2(110) is a maximal valence oxide where the occupied states are predominantly O2*p* in character and the unoccupied levels are derived from the Ti 3*d* orbitals. As a result, the information contained in UPS spectra is dominated by the anion sites while IPE results reflect the state of the cation. When the TiO_2(110) surface is reduced, the Ti ions adjacent to oxygen vacancies should be strongly affected. Figure 17 (24) shows UPS and IPE spectra from the stoichiometric and reduced TiO_2(110) surfaces. As can be seen, significant changes occur in the IPE spectrum after ion bombardment with a dose that is less than 1% of that producing the dashed UPS spectrum. Furthermore, by comparison with theoretical calculations, the enhanced intensity near 4 eV in the IPE spectrum can be directly associated with a particular oxygen vacancy structure on the surface,

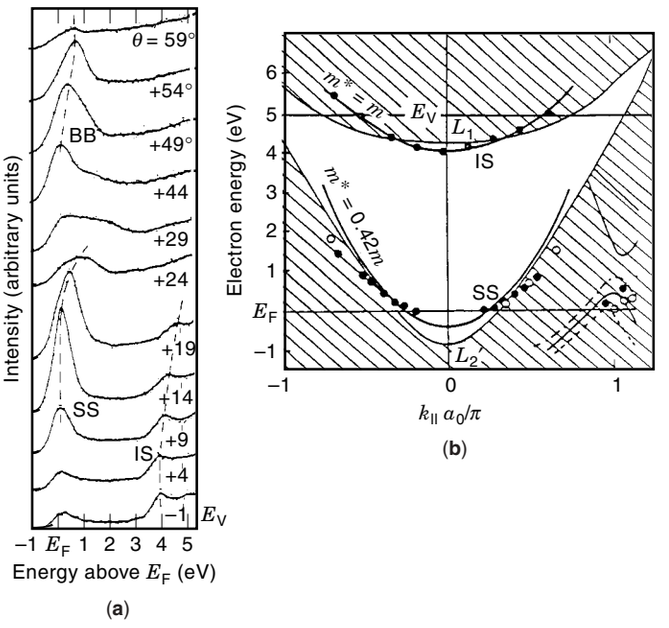

Figure 15. (a) Isochromat inverse photoemission spectra from the Cu(111) surface taken as a function of incident electron angle. The feature near 4 eV in the spectra near normal incidence is the image potential state. At larger angles, another surface state passes through the Fermi level and is observed to disperse to higher electron energy. Near 40° a second large feature emerges and is associated with the Cu bulk bands. (b) A plot of the crystal momentum parallel to the surface, $k_\parallel$, of the features in the inverse photoemission spectra of (a). The surface state (SS) and image state (IS) have very different effective masses. The bulk state near the right of the figure is well reproduced by calculations (solid lines). From Ref. (22).

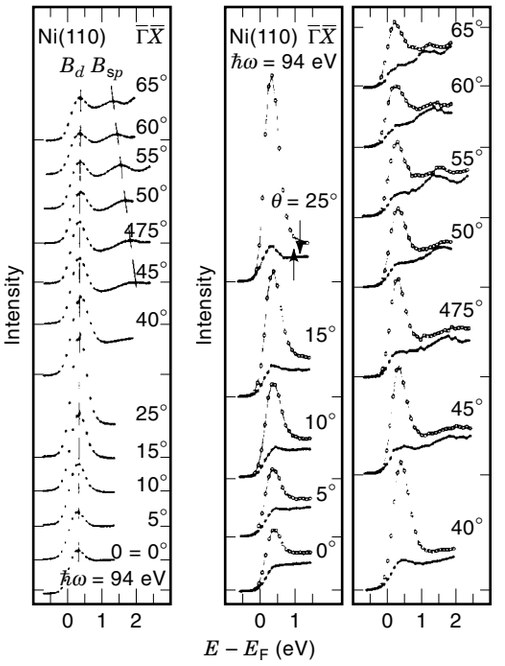

Figure 16. Spin-polarized inverse photoemission spectra from the Ni(110) surface. The left panel contains conventional IPE spectra showing a strong peak near the Fermi level that changes intensity as a function of angle. The spin-polarized spectra of the center and right panels show how this feature is essentially 100% composed of minority spin states. From Ref. (23).

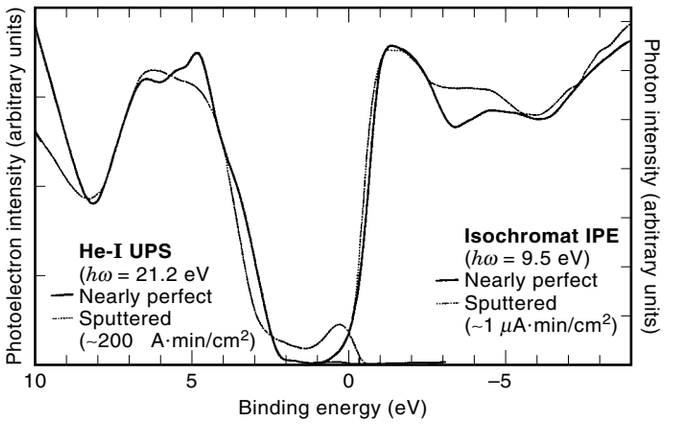

Figure 17. Direct and inverse photoemission spectra from TiO_2(110). The solid curves are for the stoichiometric surface while the dashed curves are from surfaces that are chemically reduced by ion bombardment. The feature near the Fermi level in the sputtered photoemission spectrum is related to filled Ti 3*d* levels at reduced sites, similar to the spectrum from Ti_2O_3 in Fig. 10. The excess emission near 4 eV in the inverse photoemission spectrum is associated with a specific type of oxygen vacancy. Note that the strong modification of the inverse photoemission spectrum is observed with 200 times less ion bombardment than was necessary to see a sputter-induced feature of similar intensity in the photoemission spectrum. From Ref. (24).

while the photoemission features simply indicate the presence of reduced Ti ions.

BIBLIOGRAPHY

1. T. Koopmans, *Physica 1,* **104**, 1933.
2. From A. Zangwill, *Physics at Surfaces,* Cambridge University Press, Cambridge, 1988.
3. S. LaShell, B. A. McDougall, and E. Jensen, *Phys. Rev. Lett.,* **77**: 3419, 1996.
4. D. Eastman et al., *Nucl. Instrum. Meth.,* **122**: 327, 1980.
5. S. Hüfner, in *Photoemission in Solids II,* L. Ley and M. Cardona (eds.), Springer-Verlag, Berlin, 1979.
6. D. A. Shirley, *Phys. Rev. B,* **5**: 4709, 1972.
7. A. C. Simonsen, F. Yubero, and S. Tougaard, *Phys. Rev.,* **56**: 1612, 1996.
8. S. Doniach and M. Sunjic, *J. Phys. C,* **3**: 285, 1970.
9. E. Jensen et al., *Phys. Rev. B,* **41**: 12468, 1990.
10. D. M. Riffe et al., *Phys. Rev. B,* **54**: 17118, 1996.
11. F. J. Himpsel et al., *Phys. Rev. B,* **38**: 6084, 1988.
12. J. E. Demuth and D. E. Eastman, *Phys. Rev. Lett.,* **32**: 1123, 1974.
13. T. Gustafsson and E. W. Plummer, in *Photoemission and the Electronic Properties of Surfaces,* B. Feuerbacher, B. Fitton, and R. F. Willis (eds.), Wiley, New York, 1978.
14. K. E. Smith and V. E. Henrich, *Phys. Rev. B,* **38**: 9571, 1988.
15. T-C. Chiang et al., *Phys. Rev. B,* **21**: 3513, 1980.
16. K. C. Pandey and J. C. Phillips, *Phys. Rev. B,* **9**: 1552, 1974.
17. Z. X. Shen et al., *Science,* **267**: 343, 1994.
18. E. Kisker et al., *Phys. Rev. Lett. B,* **31**: 329, 1985.
19. K. Starke et al., *Phys. Rev. B,* **53**: R10544, 1996.
20. N. B. Brookes, Y. Chang, and P. D. Johnson, *Phys. Rev. Lett.,* **67**: 354, 1991.
21. V. Dose, *Surf. Sci. Rep.,* **5**: 337, 1985.
22. S. L. Hulbert et al., *Phys. Rev. B,* **31**: 6815, 1985.
23. M. Donath, *Surf. Sci. Rept.,* **20**: 251, 1994.
24. A. K. See and R. A. Bartynski, *Phys. Rev. B,* **50**: 12064, 1994.

Further Reading

B. Feuerbacher, B. Fitton, and R. F. Willis, eds., *Photoemission and the Electronic Properties of Surfaces,* Wiley, New York, 1978.

L. Ley and M. Cardona, eds., *Photoemission in Solids I & II,* Springer-Verlag, Berlin, 1979.

E. W. Plummer and W. Eberhardt, *Adv. Chem. Phys.,* **49**: 533, 1982.

G. Ertl and J. Kuppers, *Low Energy Electrons and Surface Chemistry,* VCH, Weinheim, 1985.

C. S. Fadley et al., *Prog. in Surf. Sci.,* **54**: 341, 1997.

A. Zangwill, *Physics at Surfaces,* Cambridge University Press, Cambridge, 1988.

S. Hufner, Introduction to photoemission spectroscopy, *Springer Ser. Solid State Sci.,* **82**: Springer, Berlin, 1992.

P. D. Johnson, *Spin Polarized Photoemission,* Report on Progress in Physics, **60**: 1217–1304, 1997.

D. Briggs and M. P. Seah, *Practical Surface Analysis,* (2nd ed.), Wiley, New York, 1996.

D. Chatterji, *The Theory of Auger Transitions,* Academic Press, London, 1976.

J. C. Fuggle, in *Electron Spectroscopy: Theory, Techniques and Applications,* Vol. 4, C. R. Brundle and A. D. Baker, eds., Academic Press, London, 1981.

N. V. Smith, *Inverse Photoemission,* Reports on Progress in Physics, **51**: 1227, 1988.

V. Dose, Momentum Resolved Inverse Photoemission, *Surf. Sci. Rept.,* **5**: 337, 1985.

M. Donath, *Surf. Sci. Rept.,* **20**: 251, 1994.

D. P. Woodruff and T. A. Delchar, *Modern Techniques of Surface Science,* (2nd ed.), Cambridge University Press, Cambridge, 1994.

C. L. Briant and R. P. Messmer, eds., *Auger Electron Spectroscopy, Treatise on Materials Science and Technology, Vol. 30,* Academic Press, Boston, 1988.

ROBERT A. BARTYNSKI
Rutgers University